Article Info

Title : Debonding strength of bundled glass fibers subjected to stress pulse loading
Author : Fergyanto E. Gunawan
Journal : Engineering Fracture Mechanics 78, 2731–2745, 2011
Indexing : Thomson Reuters dan Scopus
Publisher : Elsevier
URL : http://www.sciencedirect.com/science/article/pii/S0013794411002785

Engineering Fracture Mechanics 78 (2011) 2731–2745

Contents lists available at SciVerse ScienceDirect

Engineering Fracture Mechanics

journal homepage: www.elsevier.com/locate/engfracmech

Debonding strength of bundled glass fibers subjected to stress pulse loading

Fergyanto E. Gunawan

Department of Industrial Engineering, Bina Nusantara (BINUS) University, Jl.K.H. Syahdan No. 9, Kemanggisan/Palmerah, Jakarta 11480, Indonesia

ARTICLE INFO

Article history:
Received 7 October 2010
Received in revised form 14 July 2011
Accepted 25 July 2011

Keywords:
Debonding
Fracture
Computational modeling
Finite element analysis
Cohesive zone model

ABSTRACT

This paper reports experimental results of the debonding propagation of bundled-fibers specimens subjected to a tensile stress wave. In addition, the paper also presents a dynamic debonding model for the problem on the basis of the cohesive zone model, and verifies the model by comparing the predicted debonding to the experimental data. The established numerical model is used to study the propagation mode of the debonding, and the result suggests that in this particular specimen design and loading condition, the debonding initiated in a mixed mode condition. However, the mode II quickly increased and dominated the mode I during an early debonding propagation up to certain extend where the mode mixity became constant.

1. Introduction

Damages in a composite structure may occur by various mechanisms such as fiber fracture, matrix cracking, debonding, delamination, and fiber buckling. Among those damage types, the fiber fracture possess the greatest threat to the structure integrity because the fiber plays major role in transferring the load; therefore, its failure will significantly reduce the structure load transfer capability. However, the fiber can only be effective in sustaining the load when a good bond exists in the interface of the fiber and matrix beside those interfaces between laminae in a laminated composite structure. Consequently, debonding, or decohesion along fiber–matrix interface, plays an important role in maintaining the integrity of the composite structure.

For those reasons, many systematic investigations have been performed to study the debonding despite existence of many challenges particularly in the experimental aspects. Within this respect, one major issue is related with the specimen design in which the specimen should allow one to easily produce the debonding on various loading conditions, to easily observe the debonding process, and to easily measure parameters related to the debonding.

The experiments in studying the debonding phenomenon can mainly be divided into two groups: the fiber pull-out testing method and the fiber push-out testing method. The fiber pull-out test particularly using a single fiber has been widely used with great success [1–4] on various conditions such as on a transversal loading condition [5], and on a microscopic condition using a drop of the matrix as called the microbond test method [3,4,6]. In addition, the method has also been studied analytically [7] by taking into account the friction effect [8,9], the thermal stress, and the residual stress [10]. Not only using a single fiber, the pull-out testing method has also been used in the debonding involving a bundle of fibers [11–14]. The use of a bundle instead of a single fiber is particularly interesting when dealing with a very small fiber diameter such as natural fibers. The kenaf natural fiber, for an example, only has a diameter in range of 40–70 μm [15]. Even in an experiment

E-mail addresses: fgunawan@binus.edu, f.e.gunawan@gmail.com

0013-7944/$ - see front matter © 2011 Elsevier Ltd. All rights reserved.
doi:10.1016/j.engfracmech.2011.07.008

Nomenclature

c_d	longitudinal wave speed
c_s	shear wave speed
c_R	Rayleigh wave speed
D	a damage parameter
E	Young's modulus
E_n	elastic stiffness of the interface in the normal direction
E_s	elastic stiffness of the interface in the shear direction
G_n^c	critical cohesive energy in the normal mode
G_s^c	critical cohesive energy in the shear mode
K_1	stress intensity factor of the normal mode
K_2	stress intensity factor of the shear mode
l_0	characteristic length of an interface crack
r	distance from a crack-tip
$\mathbf{T}$	traction vector
T_n	normal traction
T_s	shear traction
T_n^c	critical normal traction
T_s^c	critical shear traction
Δ_n	normal separation
Δ_s	shear separation
Δ_{mix}	mix mode separation
$\mathbf{\Delta}$	separation vector
ϵ	oscillatory index of an interface crack
ε_n	strain in the normal direction
ε_s	strain in the shear direction
μ	shear modulus
ν	Poisson's ratio
ρ	material density
σ_n	normal stress
σ_s	shear stress

involving an synthetic fiber, Ref. [16] suggested that using a bundled fibers allowed a better control and better visualization of the failure process. Therefore, a debonding test using a bundle of fibers is easier in a number of circumstances. In addition to the fiber pull-out testing method, the debonding phenomenon has also been studied by means of the fiber push-out testing method [16–18]. Ref. [17] has provided a theoretical analyses of the method, on the basis of the fracture mechanics, and has also compared the results to those of the fiber pull-out method. The fiber push-out method seems to offer a simple technique to study the debonding in dynamic loading conditions, specifically in conjunction with the Hopkinson testing method [16,18].

This paper reports experimental results of the debonding propagation on bundled-fibers specimens subjected to a tensile stress-wave. In addition, the paper also presents a dynamic debonding model by adopting the approach of Xu and Needleman [29] and verifies the model by comparing the predicted debonding against the experimental data. Finally, the established numerical model is used to study the propagation mode of the debonding.

2. Dynamic debonding experiment

2.1. Specimen

For the purpose of this study, a cylindrical-type specimen, as schematically shown in Fig. 1, was designed such that the debonding could easily be produced when a stress pulse passes through the specimen. The data related to the specimen geometry are given in Table 1.

The specimen has a bundle of glass fibers that placed along its axis. The bundle was fabricated from glass fibers where each glass fiber has a nominal diameter of 7 μm. Two types of the specimens were produced; the first type has 1 mm of the bundle diameter of glass fibers, and the second type is that of 2 mm of the bundle diameter.

The specimen was simply manufactured in the laboratory by the following process. Firstly, a tubular mold, made of an aluminum alloy, with a nominal diameter of 10 mm was prepared; then, the fiber-bundle was placed along the axis of the mold; and then, unsaturated polyester resin was poured into the mold with a great attention such that the air bubbles trapped in the specimen could be minimized. Finally, the specimen was cured at 75 °C in an autoclave for two hours and then cooled down to a room temperature.

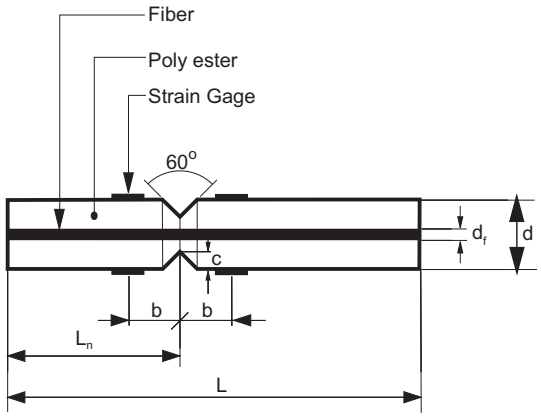

Fig. 1. Geometry of the cylindrical-type specimen.

Table 1
Geometry data in mm of the specimen.

Descriptions	Values (mm)
Length L	200
Diameter d	9.5
Diameter of the fiber-bundle d_f	1, 2
Location of the notch[a] L_n	90
Depth of the notch c	3
Gage location[b] b	20

[a] Measured from the impact-site.
[b] Measured from the notch.

Using a lathe machine, the specimen diameter was reduced to 9.5 mm; and then, a notch was made at the prescribed location. This process allowed us to produce specimens having negligible variation in diameter, which is very important to produce consistent experimental data. The notch has a depth of 3 mm, and formed an angle of 60°.

The mechanical properties of the hardened polyester and glass fiber were obtained in independent experiments. For the glass fiber, these properties were 76.0 GPa for the Young's modulus, 0.23 for the Poisson's ratio, and 1165 kg/m^3 for density. Meanwhile, for the hardened polyester, these properties are 5.4 GPa, 0.32, and 2450 kg/m^3. In addition, the longitudinal wave speed c_d, the shear wave speed c_s, and the Rayleigh wave speed c_R that defined as [19]:

$$c_d = \sqrt{\frac{E(1-v)}{\rho(1+v)(1-2v)}},$$

$$c_s = \sqrt{\frac{\mu}{\rho}}, \quad \text{and}$$

$$f(c_R) = \left[2 - \left(\frac{c_R}{c_s}\right)^2\right]^2 - 4\sqrt{\left[1 - \left(\frac{c_R}{c_d}\right)^2\right]\left[1 - \left(\frac{c_R}{c_s}\right)^2\right]} = 0,$$

where E is the Young's modulus, v is the Poisson's ratio and μ is the shear modulus were obtained as following: c_d = 8696 m/s, c_s = 5150 m/s, and c_R = 4718 m/s for the glass fiber. As for the hardened polyester, c_d = 1776 m/s, c_s = 914 m/s, and c_R = 850 m/s.

2.2. Experimental apparatus and procedures

The stress pulse was generated by striking a load transfer rod with a steel ball in a gas gun system as schematically shown in Fig. 2. Prior the experiment, the helium gas in the gas tank was pumped into the reservoir where the pressure can be controlled accurately. In the experiment, the solenoid valve was used to regulate the flow of the helium gas from the reservoir into the barrel.

The load transfer rod was made of a steel material having a length of 1 m, and a diameter of 20 mm.

Prior the test, four strain gages were glued to each specimen, and the impact-site of the specimen was attached to the end of the load transfer rod. Alignment of the load transfer rod and the specimen was carefully controlled. Among those four strain gages, two of them were placed before the notch; the others two were placed after the notch. Each pair of the strain

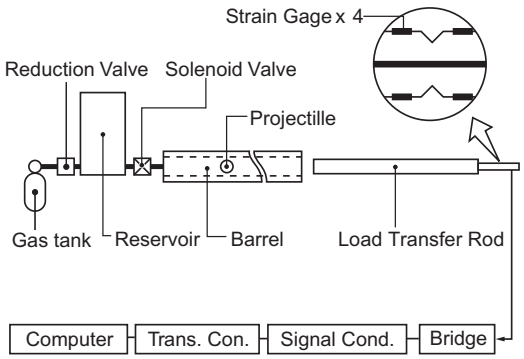

Fig. 2. The schematic diagram of the air gun impact system.

gages was connected to a Wheatstone bridge in a half-bridge configuration; hence, the strains due to the bending wave, if any, could be canceled out.

The data from the bridge were recorded in a computer via a transient converter and a signal conditioner. The signal conditioner was that of CDV/CDA-700A manufactured by Kyowa, and the transient converter was TDS-700, and is a transient memory that could sample the data at a rate of 0.1 μs.

The experimental procedures were as following: each specimen was impacted once, the strains were recorded, and then, occurrence of the debonding was firstly observed with a naked eye. The specimen having visible debonding, as typically shown in Fig. 3, was further sectioned with a fine cutter, then the debonding length was measured using a digital microscope. From the test, we established a relation between the maximum strain due to the reflected-tensile stress-wave corresponding to the debonding length.

2.3. Experimental results

The main results from experiments were the debonding length and the maximum strains of the reflected stress-wave at the rear of the notch. Those data were collected and reproduced in Fig. 4 for the 1 mm fiber-bundle specimen and in Fig. 5 for the 2 mm case. Basically, the maximum strain data were selected from the strain-history data. Typically, the strain-history data at a certain impact level are shown in Fig. 6 as a solid line. It needs to be noted that the strain depicted in the figure is associated to a case where the matrix ahead of the notch fractured completely, but the debonding has not occurred yet. At a higher impact load, the typical strain-history data are shown in Fig. 7 for 1 mm fiber-bundle and Fig. 8 for 2 mm fiber-bundle. When the impact stress was increased slightly than this level, the debonding was observed on the majority of the specimens.

3. Numerical analysis

As the experimental results, shown as circles '○' in Figs. 4 and 5, have established a relationship between a macroscopic parameter, i.e. the maximum of the strain–time history, and the debonding process parameter, i.e. the debonding length,

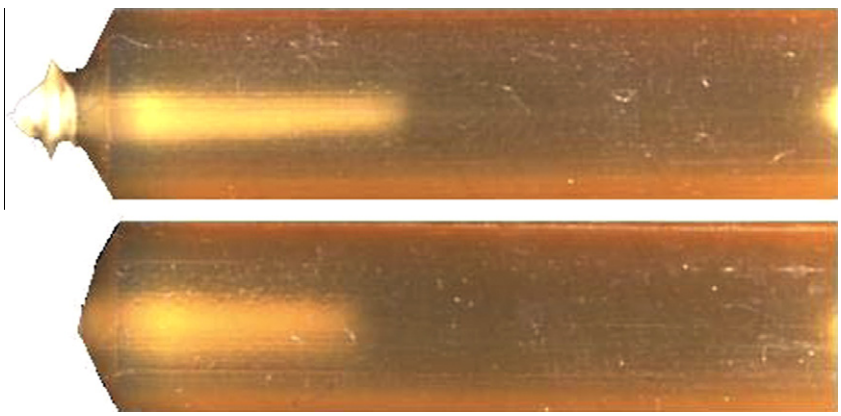

Fig. 3. The debonding on a specimen.

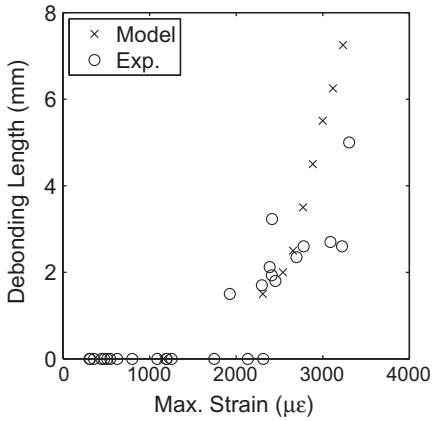

Fig. 4. The maximum strain of the reflected stress-wave at the rear gage versus the debonding length of 1 mm bundled fiber diameter specimen.

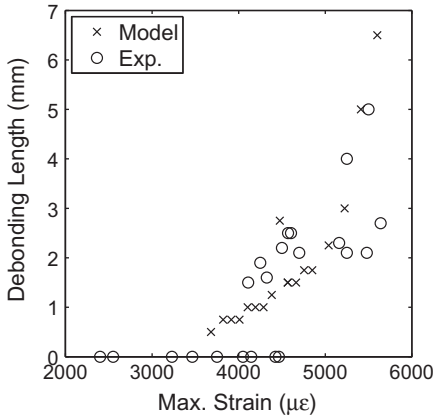

Fig. 5. The maximum strain of the reflected stress-wave at the rear gage versus the debonding length of 2 mm bundled fiber diameter specimen.

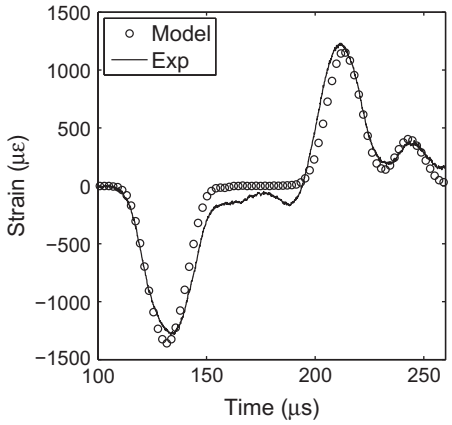

Fig. 6. The solid line is the strain–time history recorded at the rear-gage of the 1 mm bundled fiber diameter specimen when the matrix ahead of the notch fractured, and the circle '○' denotes the simulation results.

then it is necessary to establish a mechanical model that is able to link the macroscopic parameter to the debonding process. This issue will be discussed in this section. In addition, the section will also present the stress and fracture analysis of the dynamic debonding event.

The maximum of the strain–time history is selected as the primary macroscopic parameter on the basis of the following reasons: Since all the experiments were performed by use similar spherical projectiles in size and geometry, the resulted

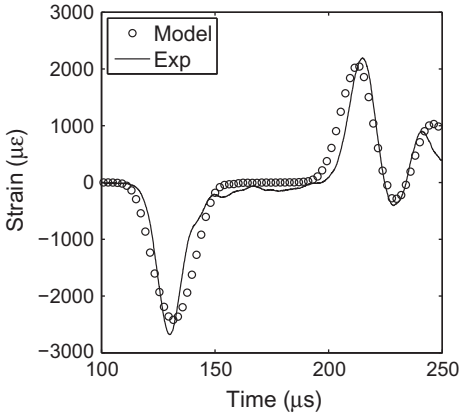

Fig. 7. The solid line is the strain–time history recorded at the rear-gage of the 1 mm bundled fiber diameter specimen when the debonding on the matrix–fiber interface was about to occur, the circle '○' denotes the simulation results.

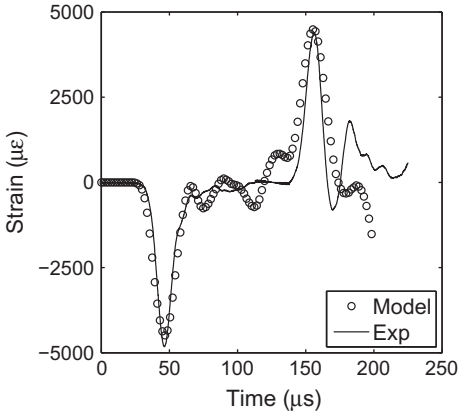

Fig. 8. The solid line is the strain–time history recorded at the front-gage of the 2 mm bundled fiber diameter specimen when the debonding occurred on the matrix–fiber, the circle '○' denotes the simulation results.

strain–time history data were essentially similar from one experiment to other in their profiles across the time, and the only differences were in their amplitudes. However, the strain time history followed an event of debonding was different than that without the debonding. The change of the projectile velocity only significantly affected the magnitude of the strain–time history data. Therefore, the maximum of the strain–time history data of the tensile reflected stress-wave were selected as a variable that determines the magnitude of the applied load.

Furthermore, the present computational model involves a phenomenological fracture model of the cohesive zone model [20–22], which was employed into the model such that the model would allow us to propagate the debonding on a prescribed direction. The same fracture model has also been adopted in Ref. [14] for a similar debonding problem but in the static loading condition. However, the problem of the interface fracture mechanics particularly in the dynamic regime is substantially more complex. The fracture toughness, for an example, is depending on the mode mixity where the experimental evidents seem to indicate the fracture toughness increases as the mode mixity increasing [23]. Furthermore, since the stress field ahead of an interface crack is not only singular but also oscillating as described by the following formula [24]:

$$\sigma_n + \jmath\sigma_s = \frac{K_1 + \jmath K_2}{\sqrt{2\pi r}} \left(\frac{r}{l_0}\right)^{\jmath\epsilon},$$

where σ_n is the normal stress, σ_s is the shear stress, K_1 and K_2 are respectively the stress intensity factors of the normal and shear modes, r is the distance from the crack-tip, l_0 is the characteristic length, and ϵ is the oscillatory index; hence, the fracture toughness will involve a definition of the characteristic length l_0, which its own definition has been a subject of interest of many researchers. Many ideas have been proposed in regard to the characteristic length: Ikeda [25] proposed the size of the process zone, Tang and Zehner [26] proposed a distance measured from the crack-tip to a point where the $\log(\sigma_n)$ crossess $\log(\sigma_s)$, Sun and Jih [27] proposed the crack length, and finally, Bjerkén and Christer [28] proposed the size of the finite element ahead of the crack-tip.

Although the interfacial fracture mechanics is complex due to a number of factors such as dependence of the energy release rate on the crack speed, the mode mixity, and the crack growth, but Xu and Needleman [29] has shown that in an interface, the crack initiates when the work of separation in the cohesive zone model equals to the generalization of Rice's *J*-integral [30,31]. This phenomenon was observed during the crack initiation and during some short interval following the initiation, but the value of *J* heavily oscillated about the work of separation at the later stage of the crack propagation where the oscillation begun at a shift from a mode I dominant to a mode II dominant, and the oscillation frequency increased with the development of the contact zone at the ahead of the crack. In spite of that fact, this particular model is interesting because it could be defined using only a few parameters but seems to be able to predict the propagation of a crack in an interface reasonably; therefore, the same approach was adopted in the present work.

3.1. Theory

In this paper, the cohesive constitutive model, or the traction–separation model [22], that relates the traction $\mathbf{T}$ to the separation $\mathbf{\Delta}$ at the interface is governed by a bilinear softening model [32] as schematically shown in Fig. 9. The both traction and separation are having two components, namely, the normal and shear components:

$$\mathbf{T} = \{ T_n \quad T_s \}^T, \quad \text{and} \quad \mathbf{\Delta} = \{ \Delta_n \quad \Delta_s \}^T, \tag{1}$$

where the subscript n denotes the normal direction and s denotes the shear or tangential direction. In addition, the superscript c denotes the critical value, which is a material constant. Therefore, T_n^c and T_s^c denote the interface normal strength and shear strength, respectively. The symbol Δ^c denotes the displacement when a complete separation occurs.

In this paper, the cohesive model is implemented on zero thickness elements; therefore, the nominal strains can be defined as

$$\varepsilon_n = \Delta_n, \quad \text{and} \quad \varepsilon_s = \Delta_s. \tag{2}$$

The elastic part of the traction–separation model can then be written as

$$\mathbf{T} = \begin{Bmatrix} T_n \\ T_s \end{Bmatrix} = \begin{bmatrix} E_n & 0 \\ 0 & E_s \end{bmatrix} \begin{Bmatrix} \varepsilon_n \\ \varepsilon_s \end{Bmatrix} = \mathbf{E}\boldsymbol{\varepsilon}, \tag{3}$$

where the normal and shear deformations are uncoupled. The symbols E_n and E_s denote the elastic moduli for the normal and shear modes, respectively.

The cohesive zone model basically combines strength-based analysis with fracture mechanics to predict the debonding initiation and to predict the debonding propagation. In the current approach, the debonding is assumed to initiate when a quadratic interaction involving the nominal stress ratios reaches one, or mathematically speaking:

$$\left\{ \frac{\langle T_n \rangle}{T_n^c} \right\}^2 + \left\{ \frac{T_s}{T_s^c} \right\}^2 = 1, \tag{4}$$

where $\langle \cdot \rangle$ is the Macaulay brackets that set any negative values to zero. Hence, a pure compression deformation or stress state does not initiate debonding. However, when the debonding has initiated by an amount of D, where $0 \leqslant D \leqslant 1$, the material strengths degrade to:

$$T_n = \begin{cases} (1-D)\overline{T}_n, & \overline{T}_n \geqslant 0 \\ \overline{T}_n & \text{otherwise} \end{cases} \tag{5}$$

for the normal traction, and to

$$T_s = (1-D)\overline{T}_s \tag{6}$$

for the shear traction. The symbols $\overline{T}_n$ and $\overline{T}_s$ are the stress components predicted by the elastic traction–separation behavior for the current strains without debonding.

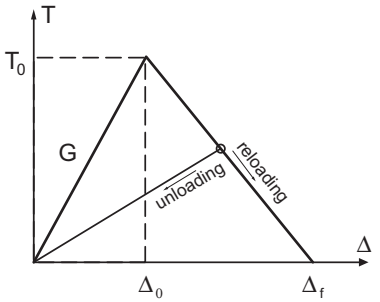

Fig. 9. The bilinear traction–separation model.

The debonding variable D is computed by

$$D = \frac{\Delta^c_{\text{mix}}\left(\Delta^{\max}_{\text{mix}} - \Delta^0_{\text{mix}}\right)}{\Delta^{\max}_{\text{mix}}\left(\Delta^c_{\text{mix}} - \Delta^0_{\text{mix}}\right)}, \tag{7}$$

where those mix mode displacements are computed by

$$\Delta_{\text{mix}} = \sqrt{\langle \Delta_n \rangle^2 + \Delta_s^2}. \tag{8}$$

In Eq. (7), the Δ^0_{mix} denotes the displacement at the onset of damage, and the Δ^c_{mix} denotes the displacement when complete separation has occurred. The both Δ^0_{mix} and Δ^c_{mix} can be easily derived from the cohesive model parameters of the elastic modulus, the critical cohesive strength, and the critical cohesive energy. The $\Delta^{\max}_{\text{mix}}$ refers to the maximum value of the effective displacement attained during the loading history.

Therefore, as can be also seen in Fig. 9, after the onset of debonding Δ^0, the interface strengths in both the normal and shear modes gradually decrease to zero. The area under the traction–separation curve is the critical cohesive energies, G^c_n and G^c_s:

$$\int_0^{\Delta_n} T_n(\Delta_n) d\Delta_n = G^c_n, \tag{9}$$

for the normal mode, and

$$\int_0^{\Delta_s} T_s(\Delta_s) d\Delta_s = G^c_s, \tag{10}$$

for the shear mode. The critical cohesive energy on the mix mode can be defined based on a power law fracture criterion:

$$\left\{\frac{G_n}{G^c_n}\right\}^{\alpha} + \left\{\frac{G_s}{G^c_s}\right\}^{\alpha} = 1. \tag{11}$$

The power law criterion with $\alpha = 1$ was found to be suited to predict failure of thermoplastic matrix composites because the results were comparable to the more sophisticated criteria, while using fewer independent variables [21]; therefore, in this study, the α is assumed to be equal to one.

This mechanical model assumes the debonding or the de-cohesion process as the only dissipative mechanism and ignores the fact that the energy may also be dissipated due to strain-rate dependency (material viscoelasticity or viscoplasticity) and local-scale temperature rise among others. Regarding the material viscoelasticity, some separated tests using long rod specimens (as long as 0.5–1 m) made of the same material have shown that the mechanism significantly affected the strain–time history. However, when the specimen is short like the one used in the present study, the viscoelasticity has rather negligible effect as shown by the strain history data. In addition, we attached the strain-gage at 20 mm away from the notch where the fracture took place. We expect within this close distance, the elastic assumption should provide a good approximation of the viscoelastic material. Regarding the local-scale temperature rise, the model assumes its magnitude is significantly smaller than the energy required to produce the debonding. Besides, it is rather difficult to take into account this factor considering the material is not a good conductor.

3.2. The finite element model and fracture parameters

The finite element method was used to establish a mechanical model that relates the maximum strain to the debonding length. Fig. 10 shows the finite element mesh around the notch. We evaluated three finite element models as tabulated in Table 2. Model 2 was by obtained by broken down each element in Model 1 into four similar elements. Using the same procedure, Model 3 was derived from Model 2.

All of those models were utilized in the study; however, only Model 3 provided results that match the experimental data reasonably well on various conditions, from the onset of the debonding until its final position and for the both specimen types. Therefore, only the results of Model 3 were presented in the paper.

To anticipate occurrence of the debonding and matrix fracture, zero thickness cohesive elements were implemented along the lines denoted by matrix–matrix interface and fiber–matrix interface in the figure. The cohesive elements in the matrix–matrix interface were employed to anticipate the matrix fracture; and in the meantime, the same type of elements in the fiber–matrix interface was for the debonding. Clearly, this approach assumed the fracture process zone occurred along a prescribed line.

The applied load was a pressure that applied uniformly across the area on the left end of the specimen. The pressure varied in time following a sine function where its peak and period were adjusted such that the strain–time history of the model matched well to those recorded in the experiment.

It is clear that the maximum strain at a point associated with the measurement point could easily be obtained from the model. As for the debonding length, we adopted an approach by Shet and Chandra [20], whose defined the cohesive crack-tip as a point in the interface where the normal traction reaches its critical value.

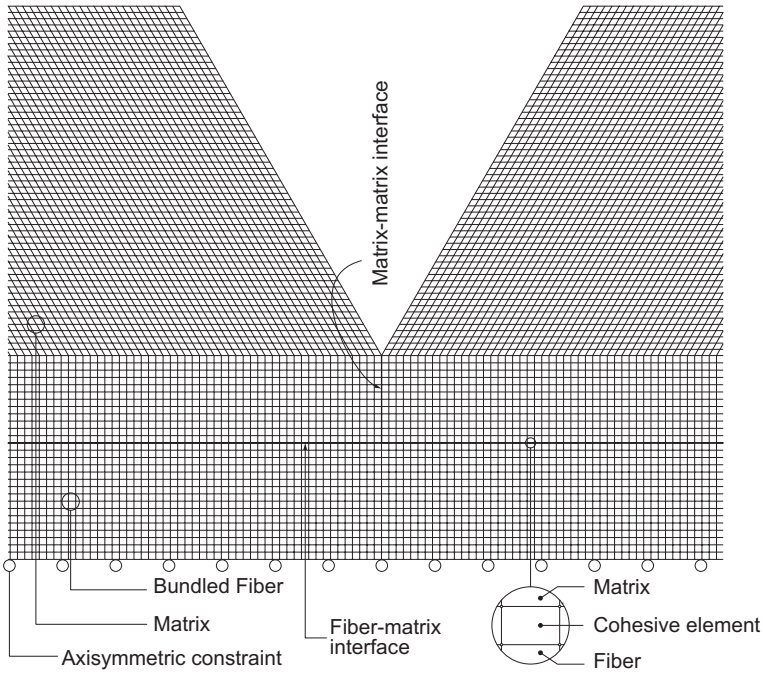

Fig. 10. The axisymmetric finite element mesh model around the notch of the bundled fiber specimen and the applied constraints.

Table 2
Three evaluated models.

	Number of elements	Number of nodes	Element length (mm)
Model 1	17,603	18,440	2.50×10^{-1}
Model 2	144,808	146,897	1.25×10^{-1}
Model 3	272,013	275,355	6.25×10^{-2}

The identification of the cohesive zone model's parameters—the strength and the critical cohesive energy—were performed in two steps. Those parameters related to the cohesive zone model in the matrix–matrix interface were established in the first step, and followed by the calibration for the parameters of the fiber–matrix interface. The calibration of those material parameters were completely performed on the basis of the data obtained from the tests of the 1 mm fiber-bundle specimens.

In the first step, initially we set the strength and the critical cohesive energy of all interfaces—the matrix–matrix interface and the fiber–matrix interface—to high values such that fracture or debonding would not take place upon an application of the impact pressure. Then, we applied a pressure having a magnitude slightly lower than that required to break the matrix–matrix interface obtained in the experiment. From this study, we registered the maximum stress on the matrix–matrix interface, and assumed the maximum stress to be equivalent with the strength of the matrix–matrix interface. We incorporated the matrix–matrix interface strength into the model, and applied the pressure that fractured the matrix–matrix interface. Finally, we reduced the cohesive energy subsequently until all elements in the matrix–matrix interface broke completely at once, and we assumed this cohesize energy to be equivalent with the critical cohesive energy of the matrix–matrix interface.

In the second step, we incorporated the above material data into the model. Then, we applied a pressure, slightly lower than the pressure required to initiate debonding that obtained in the experiment, and registered the maximum stress on the fiber–matrix interface. This value was taken as the strength of the fiber–matrix interface, and was subsequently incorporated into the model. Finally, we adjusted the fiber–matrix cohesive energy until the predicted debonding length matching the experimental data for various pressure magnitudes. This final analysis gave us the critical cohesive energy of the fiber–matrix interface.

The calibration results: for the matrix–matrix interface, the tensile strength was 72 MPa, and the critical cohesive energy in tension was 2 MPa mm; for the fiber–matrix interface: the tensile strength was 54 MPa, the shear strength was 67 MPa, and the critical cohesive energy was 2 MPa mm for the both modes. Although a dominant mixed mode fracture occurred on the fiber–matrix interface, but the matrix–matrix interface fractured in a pure normal mode.

3.3. Discussion

In this section, we discuss the model predictions, comparisons to the experimental data, and the deformation and stress state during the debonding propagation.

Fig. 6 shows the strain–time history calculated by the finite element analysis and those obtained from the experiments for the 1 mm bundled fiber diameter. The duration of the applied pressure, its magnitude, and the cohesive zone model's parameters were adjusted such that the strain–time history of the model matched reasonably well to the experimental data particularly when the stress-waves passed through the measurement points. The figure clearly shows that the model slightly over predicted the magnitude of the compressive stress-wave, slightly under predicted the magnitude of the reflected tensile stress-wave, but the model prediction fairly deviated from the measured strain–time history along an interval time between the time of the compressive stress-wave and that of the tensile stress-wave. In this particular interval, the model prediction resembled a result of an idealized specimen where the diameter of the bundled fiber is uniform across the specimen length, and the bundled is perfectly align to the specimen axis; which were extremely difficult to achieve during the manufacturing of the specimen. As for the 2 mm bundled fiber specimen, the comparison is shown in Fig. 8. For this case, a significant deviation exists during the unloading duration; however, good agreements were obtained during the compressive and tensile

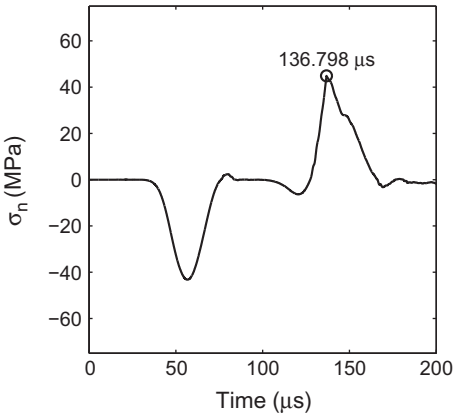

Fig. 11. The normal stress–time history at a point on the interface ahead of the notch where the debonding was initiated.

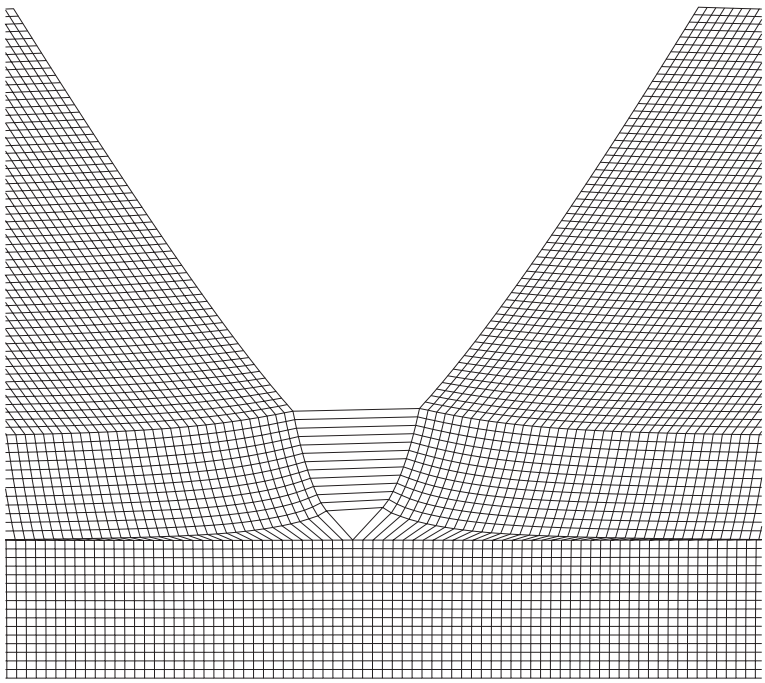

Fig. 12. The deformation around the notch area.

loadings. In spite of those deviations, the model successfully reproduced the stress propagation in the specimen during the experiment.

Besides Figs. 6, 4 also compares the experimental data to the analysis results for the 1 mm bundled fiber diameter. Using those experimental data, depicted as '○' in the figure, the cohesive zone model's parameters were adjusted to best match the model predictions to the experimental data. One should note that the maximum strains in the figure are those associated

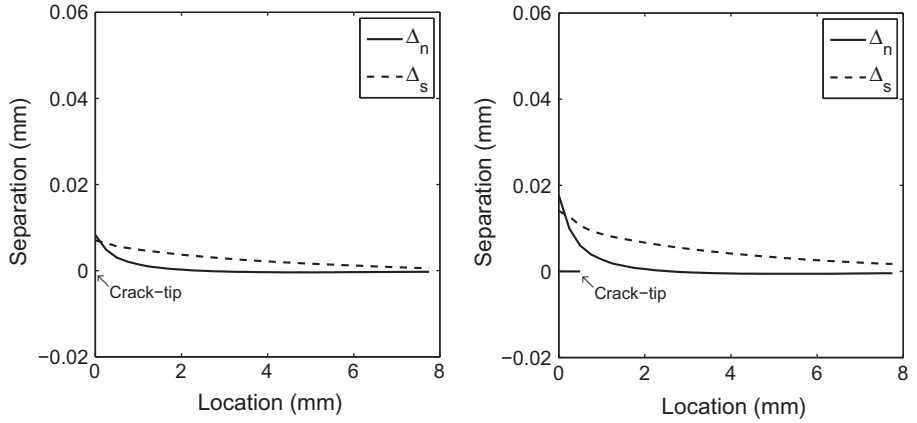

Fig. 13. The normal Δ_n and tangential Δ_s separations at time 136.9 μs and 140.2 μs.

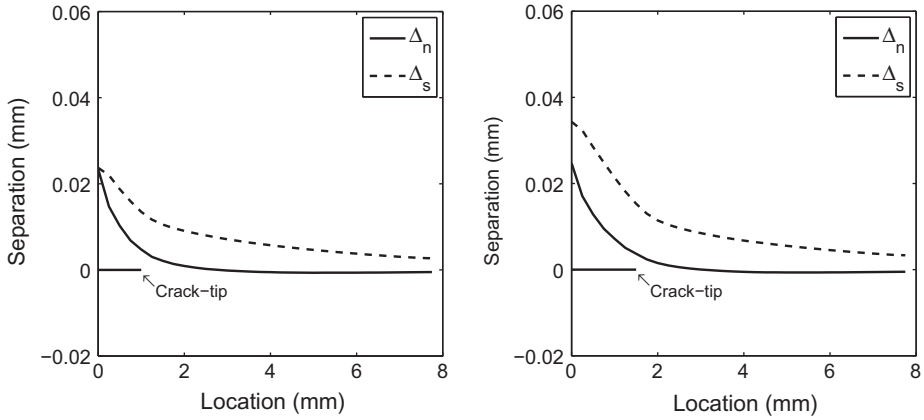

Fig. 14. The normal Δ_n and tangential Δ_s separations at time 142.6 μs and 144.3 μs.

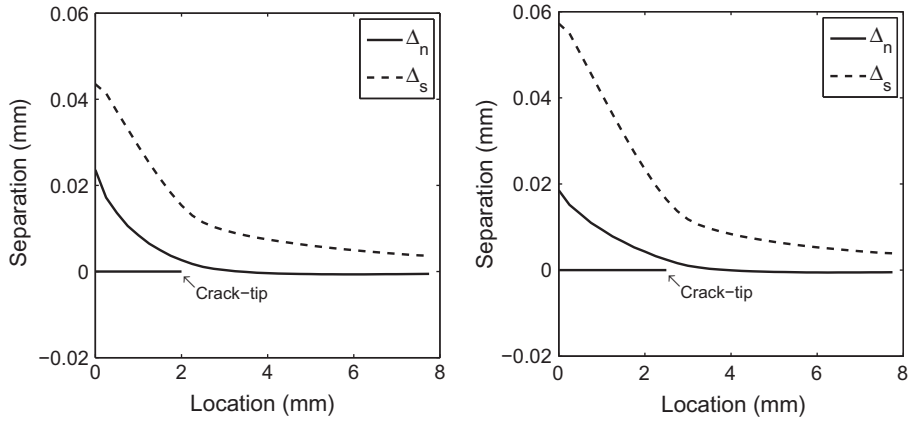

Fig. 15. The normal Δ_n and tangential Δ_s separations at time 145.6 μs and 147.4 μs.

with the reflected tensile stress-waves. In this comparison, unlike the comparison of the strain–time history, reasonable deviations existed between those two data. The deviations were mainly due to scattering of the maximum strain and debonding length data obtained from the experiments; meanwhile, the relation between the maximum strain and the debonding length obtained from the model was more consistent. However, from a statistical point of view, the experimental

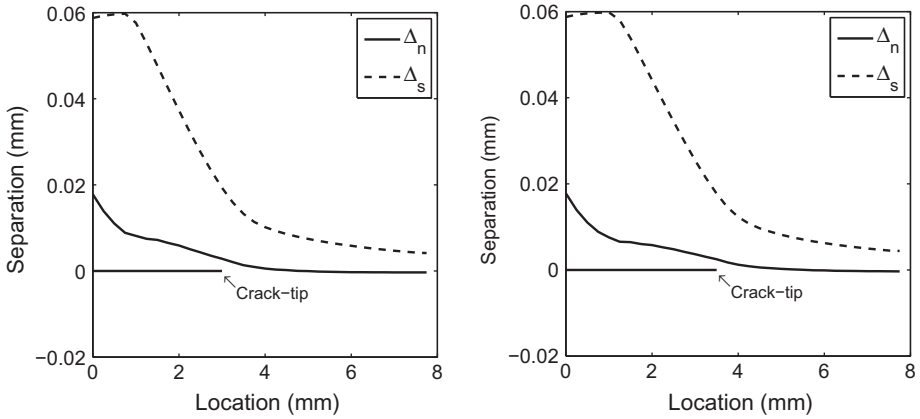

Fig. 16. The normal Δ_n and tangential Δ_s separations at time 150.0 μs and 152.0 μs.

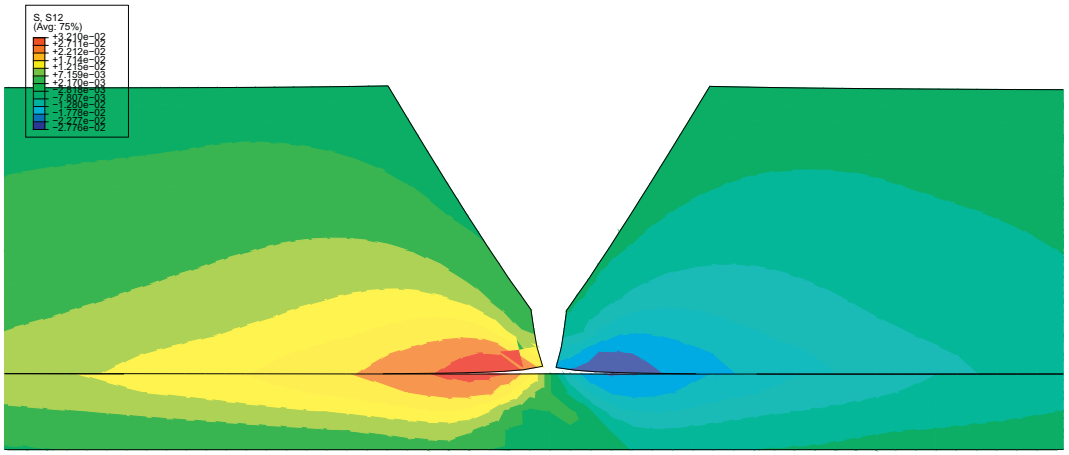

Fig. 17. The shear component of the Cauchy stress at a time of 136.9 μs.

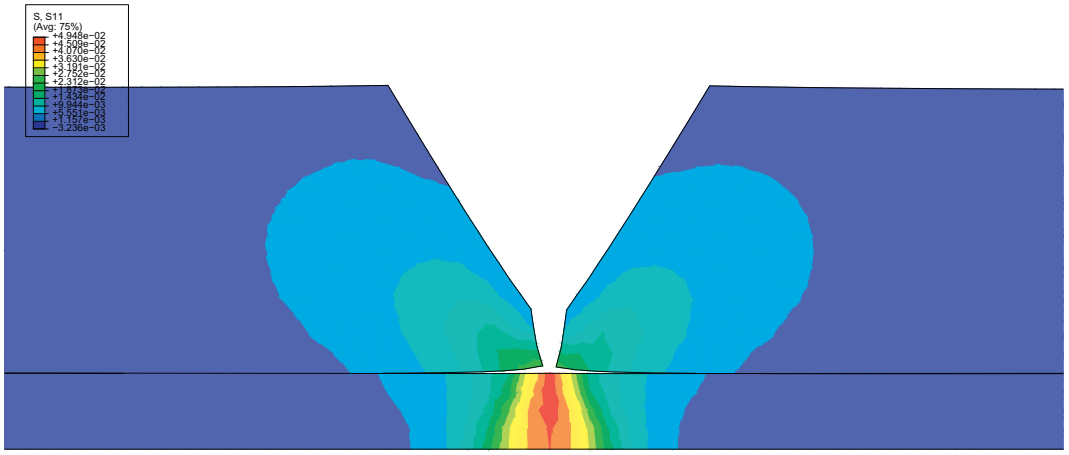

Fig. 18. The normal component of the Cauchy stress at a time of 136.9 μs.

data seems to scatter around the model predicted data within an acceptable band. Therefore, we concluded the model acceptably predicted the debonding experiment for the case of 1 mm bundled fiber specimen.

The final comparison is shown in Fig. 5 where the relation between the maximum strain and the debonding length obtained from the experiment of the 2 mm bundled fiber diameter were plotted beside those of the model predictions. The experimental data were also scatter similar to the data of the previous case. However, the model predicted data shown a stair-like phenomenon due to the finite element approach in the debonding propagation. Regardless of this fact, the model also reasonably reproduced the experimental data for the 2 mm bundled fiber diameter.

In many studies on composite fractures particularly due to a low velocity impact, the applied energy often becomes a parameter of interest related to the fracture. However, in the current case, the amount of the applied energy is rather proportional to the maximum strain. Therefore, Figs. 4 and 5 also provide an insight on effect of the applied energy to the debonding length.

The reflected tensile stress-wave reached the notch ligament at about 126 μs as shown by the stress–time history in Fig. 11. Shortly after that time, at about 136.8 μs the debonding had initiated at the interface of the bundled fiber and the matrix; Fig. 12 shows an amplified deformation around the notch at this instant.

The analysis indicated that the debonding propagated in a short time interval; started at 136.9 μs and finished at 152.8 μs. Furthermore, the analysis also revealed the mode of deformation during the debonding propagation. Figs. 13–16 reproduced the separations, in the normal and tangential directions, of the interface of the bundled fiber and the matrix at some instants on the interval. The debonding in the interface initiated and propagated in following manners:

Prior the matrix–matrix interface fractured, the tangential separation at a point on the fiber–matrix interface in front of the notch root was very small, significantly smaller than the normal separation. However, when the matrix–matrix interface fractured such that the crack which initiated at the notch root had propagated to the fiber–matrix interface, the tangential separation at this point suddenly increased to a magnitude comparable to the normal separation as shown in the left panel in

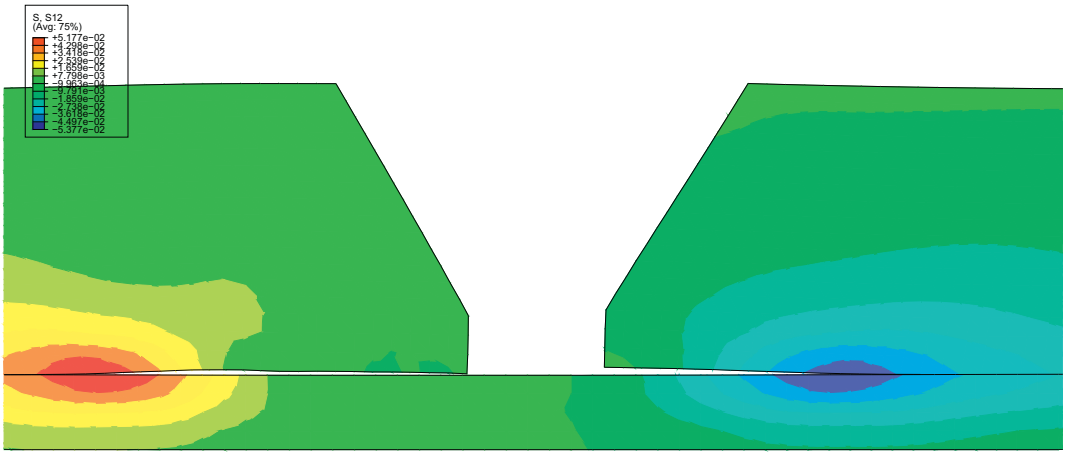

Fig. 19. The shear component of the Cauchy stress at a time of 150.0 μs.

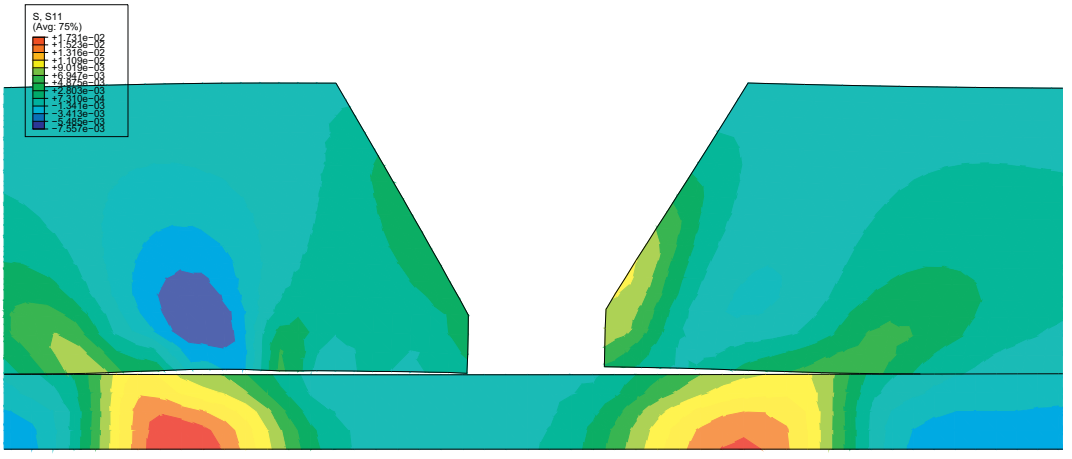

Fig. 20. The normal component of the Cauchy stress at a time of 150.0 μ.

Fig. 13. One should note that the crack-tip location was measured from a plane where the root of the notch was located. Therefore, when the crack-tip was located at 0.0 mm, the crack propagated in a mixed mode where the mode I was slightly bigger than the mode II (see the left panel of Fig. 13). However, the mode II contribution quickly increased; and when the crack length had reached 0.5 mm as shown in the right panel of Fig. 13, the mode II had dominated the mode I by a factor about two. The mode II continuously increased as depicted in Figs. 14 and 15, while the mode I was relatively constant until the crack reached a length of 2.5 mm. From this instant forward, the debonding propagated nearly at a constant mode mixity where the mode II dominated the mode I as shown in Fig. 16.

The analysis also provided the rate of the debonding propagation. The debonding initially grew at a rate about 15% of the Rayleigh wave speed of the hardened polyester, steadily increased to reach the maximum speed at about 50% of the Rayleigh wave speed, quickly decreased, and finally stopped at a crack length of 3.75 mm.

The stress field around the notch at an instant of 136.9 μs is reproduced in Fig. 17 for the shear stress and in Fig. 18 for the normal stress. For an instant of 150.0 μs, the stress field is reproduced in Figs. 19 and 20.

The both shear and normal stresses on the fiber–matrix interface were low before the matrix ahead of the notch fractured. When the matrix had fractured at 136.9 μs, the both stresses suddenly increased, but their magnitudes were relatively comparable. Along the debonding propagation, the shear stress around the crack-tip quickly increased but the normal stress decreased and then steadied at a fraction of the maximum shear stress.

4. Conclusions

This research on the debonding strength of bundled glass fibers subjected to stress pulse loading has provided an insight of the debonding initiation and propagation along the interface of the bundled fibers and the hardened polyester. On the basis of the finite element method and the cohesive zone model, a mechanical model has been established and used to study the debonding propagation. The model parameters were adjusted such that the model responses matched well to the experimental data. The mechanical model revealed that the debonding on the interface was initiated at a condition where the mode I component slightly dominated the mode II. However, upon the propagation of the debonding, the mode II component quickly increased and dominated the mode I; and finally, the ratio of the mode II to the mode I became a constant when the debonding reached certain length. Although the cohesive zone model was very simple, but a comparison of the model prediction to the experiment data suggested the cohesive zone model provided an acceptable prediction regardless the fact that the interfacial fracture mechanics is a complex issue.

Acknowledgments

The experimental results presented in this paper were collected by Ms. Fenny T. Kurniawati and Mr. Motoharu Yamauchi at Department of Mechanical Engineering of Toyohashi University of Technology. Currently, Fenny is at Musashi Seimitsu Industry Co. Ltd. in Toyohashi, Japan, and Yamauchi is at Dainippon Screen MFG. in Kyoto, Japan.

References

[1] Favre J-P, Merienne M-C. Characterization of fibre/resin bonding in composites using a pull-out test. Int J Adhes Adhes 1981;1(6):311–6. doi:10.1016/0143-7496(81)90025-7.
[2] Kim J-K, Baillie C, Mai Y-W. Interfacial debonding and fiber pull-out stresses—Part 1: Critical comparison of existing theories with experiments. J Mater Sci 1991;27:3143–54.
[3] Schuller T, Becker W, Lauke B. Analytical and numerical calculation of the energy release rate for the microbond test. J Adhes 1999;70:33–56.
[4] Liu CH, Naim JA. Analytical and experimental methods for a fracture mechanics interpretation of the microbond test including the effect of friction and thermal stresses. Int J Adhes Adhes 1999;19:59–70.
[5] Zhang H, Ericson ML, Varna J, Berglund LA. Transverse single-fiber test for interfacial debonding in composites: 1. Experimental observations. Composites: Part A 1997;28A:309–15.
[6] Hann LP, Hirt DE. Simulating the microbon technique with macrodroplets. Compos Sci Technol 1995;54:423–30.
[7] Noda N-A, Shirao R, Li J, Sugimoto J-S. Intensity of singular stress fields causing interfacial debonding at the end of a fiber under pullout force and transverse tension. Int J Solid Struct 2007;44:4472–91.
[8] Evans AG, He MY, Hutchinson JW. Interface debonding and fiber cracking in brittle matrix composites. J Am Ceram Soc 1989;72(12):2300–3.
[9] Hutchinson JW, Jensen HM. Models of fiber debonding and pullout in brittle composites with friction. Mech Mater 1990;9:139–63.
[10] Nairn JA, Liu C-H, Mendels DA, Zhandarov S. Fracture mechanics analysis of the single-fiber pull-out test and the microbon test including the effect of friction and thermal stresses. In: Proceeding 16th annual technology conference of the american society of composites; 2001.
[11] Wells JK, Beaumont PWR. Debonding and pull-out processes in fibrous composites. J Mater Sci 1985;20:1275–84.
[12] Gunawan FE, Homma H, Yamauchi N, Kuriniawati FT. Dynamic interface debonding between a glass fiber bundle and a matrix. In: Proceeding of the 2002 annual meeting of JSME/MMD, Yamaguchi, Japan; 2002. p. 667–8.
[13] Gunawan FE, Homma H, Kurniawati FT, Yamauchi M. Static debonding initiation stress of fiber glass composite. JSME Int J, Ser A 2004;47(2):122–9.
[14] Gunawan FE, Homma H, Shirley S. An analysis of debonding along interface of bundled fibers and matrix. J Solid Mech Mater Engng 2008;2:310–8.
[15] Xue Y, Du Y, Elder S, Sham D, Horstemeyer M, Zhang J. Statistical tensile properties of kenaf fibers and its composites, in: 9th International conference on wood and biofiber plastic composites; 2007.
[16] Bi X, Li Z, Geubelle PH, Lambros J. Dynamic fiber debonding and frictional push-out in model composite systems: numerical simulations. Mech Mater 2002;34:433–46.
[17] Zhou L-M, Mai Y-W, Ye L. Analyses of fiber push-out test based on the fracture mechanics approach. Compos Engng 1995;5(10–11):1199–219.
[18] Li Z, Bi X, Lambros J, Geubelle PH. Dynamic fiber debonding and frictional push-out in model composites systems: experimental observations. Exp Mech 2002;42(3):417–25.
[19] Rahman M, Michelitsch T. A note on the formula for the rayleigh wave speed. Wave Motion 2006;43:272–6.

[20] Shet C, Chandra N. Analysis of energy balance when using cohesive zone models to simulate fracture processes. Trans ASME: J Engng Mater Technol 2002;124:440–50.
[21] Camanho PP, Davila CG. Mixed-mode decohesion finite elements for the simulation of delamination in composite materials. Tech rep NASA/TM-2002-211737, NASA Langley Research Center, Hampton, VA 23681-2199; June 2002.
[22] ABAQUS analysis user's manual version 6.8.
[23] Hutchinson JW, Suo Z. Mixed mode cracking in layered materials. Adv Appl Mech 1992;29:69–191.
[24] Erdogan F. Stress distribution in bonded dissimilar material with cracks. Trans ASME Ser E: J Appl Mech 1963;32:1963.
[25] Ikeda T, Miyazaki N. Mixed mode fracture criterion of interface crack between dissimilar materials. Engng Fract Mech 1998;59(6):725–35.
[26] Tang S, Zehnder AT. Nickel–alumina interfacial fracture toughness using thick foil technique. Engng Fract Mech 2002;69:701–15.
[27] Sun CT, Jih CJ. On strain energy release rates for interfacial cracks in bimaterial media. Engng Fract Mech 1987;28:13–20.
[28] Bjerkén C, Christer P. A numerical method for calculating stress intensity factors for interface cracks in bimaterials. Engng Fract Mech 2001;68:235–46.
[29] Xu XP, Needleman A. Numerical simulation of dynamic crack growth along an interface. Int J Fract 1996;74:289–324.
[30] Rice JR. A path independent integral and the approximate analysis of strain concentration by notches and cracks. J Appl Mech 1968;35:379–86.
[31] Nakamura T, Shih CF, Freund LB. Computational methods based on an energy integral in dynamic fracture. Int J Fract 1985;27:229–43.
[32] Geubelle PH, Baylor J. The impact-induced delamination of laminated composites: a 2D simulation. Composites: Part B 1998;29B:589–602.